Experimentally confirmed design guidelines for passively *Q*-switched microchip lasers using semiconductor saturable absorbers

G. J. Spühler, R. Paschotta, R. Fluck, B. Braun, M. Moser, G. Zhang, E. Gini, and U. Keller

Ultrafast Laser Physics, Institute of Quantum Electronics, Swiss Federal Institute of Technology, ETH Hönggerberg—HPT, CH-8093 Zürich, Switzerland

Received July 10, 1998; revised manuscript received October 5, 1998

We present a model for passively *Q*-switched microchip lasers and derive simple equations for the pulse width, repetition rate, and pulse energy. We experimentally verified the validity of the model by systematically varying the relevant device parameters. We used the model to derive practical design guidelines for realizing operation parameters that can be varied in large ranges by adoption of the parameters of the semiconductor saturable-absorber mirror and choice of the appropriate gain medium. Applying these design guidelines, we obtained 37-ps pulses, which to our knowledge are the shortest pulses ever generated in a passively *Q*-switched solid-state laser. © 1999 Optical Society of America [S0740-3224(99)00503-2]

OCIS codes: 140.3480, 140.3540, 140.3580, 140.3530, 140.3500, 160.6000.

1. INTRODUCTION

Many applications require compact and simple single-mode lasers that emit subnanosecond pulses with high pulse energies and peak powers in a diffraction-limited output beam. Diode-pumped passively *Q*-switched microchip lasers are solid-state lasers that are promising sources to satisfy these requirements. The microchip cavity is extremely simple and compact, consisting of a thin disk gain medium sandwiched between the cavity mirrors.[1] The stability of the resonator with two flat mirrors is provided by a pump-induced thermal lens, thermal expansion, and gain guiding. The extremely short cavity length of several hundred micrometers enables the laser to oscillate on a single longitudinal mode and allows for pulse widths well below 1 ns in *Q*-switched operation.

As the *Q*-switching element we use a semiconductor saturable-absorber mirror (SESAM),[2–4] which simply replaces one end mirror of the microchip laser. In comparison with other saturable absorbers, e.g., doped bulk crystals,[5,6] the SESAM allows for significantly shorter cavity lengths and therefore shorter pulses. In addition, the SESAM can be adapted to different laser wavelengths. We have already demonstrated passively *Q*-switched microchip lasers in several wavelength regions.[7–9]

In this paper we present a simple model for passively *Q*-switched microchip lasers. In Section 2 we derive simple equations for the basic operating parameters. In Section 3 a comprehensive set of experimental data is shown to agree well with these equations. The flexibility of the SESAM approach allowed for a thorough check of the model. Finally, in Section 4 we give practical design guidelines for passively *Q*-switched microchip lasers, addressing different objectives for their performance.

We also have demonstrated single-frequency *Q*-switched pulses as short as 37 ps with a diode-pumped $Nd:YVO_4$ microchip laser (Fig. 1). These are, to our knowledge, the shortest *Q*-switched pulses ever obtained from a solid-state laser. Pulse widths below 100 ps at peak powers exceeding 5 kW make these microchip lasers interesting for a variety of applications, such as in medicine, light detection, and ranging (lidar) and in nonlinear frequency conversion.

2. THEORY

The history of *Q* switching goes back to 1961, when Hellwarth[10] predicted that a laser could emit short pulses if the losses of an optical resonator were rapidly switched from a high to a low value. The experimental proof was produced a year later.[11,12] Subsequently, theories have been established, first for rapid *Q* switching (instantly switched intracavity loss, with two rate equations for the photon density and the inversion),[13,14] and then for the case of passive *Q* switching,[15,16] by introduction of a third rate equation for the saturable absorber. Motivated by their research with *Q*-switched microchip lasers,[17] Zayhowski and Kelley analyzed the rate equations for rapid *Q* switching.[18] In 1995, Degnan extended the work of Erickson and Szabo for passive *Q* switching,[19] optimizing the output coupler for maximum pulse energy by using the Lagrange multiplier technique.

Here we present simple derivations for the relevant quantities in a passively *Q*-switched microchip laser, namely, pulse width, pulse energy, peak power, and repetition rate. We verify these results in Section 3 with experimental data and in Section 4 derive simple design guidelines for pulsed microchip lasers that use SESAM's.

A. Model

We consider a microchip laser cavity consisting of a crystal (or glass) of length L_g to provide a time-dependent

 © 1999 Optical Society of America

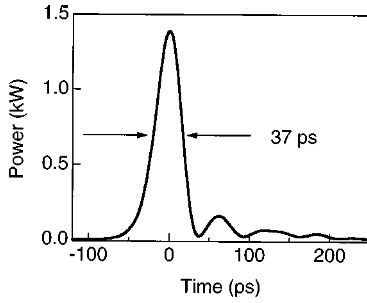

Fig. 1. Oscilloscope trace of the single-frequency 37-ps Q-switched pulse with a peak power of 1.4 kW and a repetition rate of 160 kHz.

round-trip intensity gain coefficient $g(t)$; a saturable absorber giving a saturable loss coefficient $q(t)$ (i.e., unbleached value q_0 and bleached value 0); an output coupler with transmission T_{out} and output coupling coefficient l_{out}, defined by $T_{\text{out}} = 1 - \exp(-l_{\text{out}})$; and a parasitic loss coefficient l_p (which is usually dominated by the nonsaturable loss of the SESAM). l_{out} and l_p determine the total nonsaturable loss coefficient per round trip, $l = l_{\text{out}} + l_p$. The saturation energy E_A of the absorber is assumed to be small compared with the saturation energy of the gain medium E_L. As the gain and loss are usually not more than a few percent per round trip, we can represent the intracavity power by a single quantity $P(t)$ [gain factor $G = \exp(g) \approx 1 + g$ for $g \ll 1$; losses $L = 1 - \exp(-l) \approx l$ for $l \ll 1$]. We neglect spatial hole burning, which alters the saturation of the gain and causes a spatial variation of the inversion that can lead to multiple-longitudinal-mode output.[20,21] The transverse beam profiles of the pump and the laser modes are approximated by top-hat functions of equal area A, although deviations from this generalization will have to be discussed in Section 3. For the case of a microchip laser the beam cross sections in the absorber and in the gain material are equal. This limitation is discussed in Subsection 4.A.

B. Pulse Energy

It is illustrative to derive an equation for the pulse energy by referring to the reduction of the gain during the evolution of a pulse (without using rate equations). The stored energy in the pumped gain material is proportional to the excitation density N_2, the photon energy $h\nu_L$ at the lasing wavelength, and the pumped volume AL_g:

$$E_{\text{stored}} = AL_g N_2 h\nu_L . \tag{1}$$

In the case of Q-switched microchip lasers using SESAM's, the length L_g of the gain medium is nearly equal to the cavity length (Section 3 below). In a standing-wave cavity the intensity gain coefficient per round trip is $g = 2\sigma_L N_2 L_g$, where σ_L is the emission cross section of the laser material. Thus we arrive at the following expression for the stored energy:

$$E_{\text{stored}} = \frac{h\nu_L}{2\sigma_L} Ag = E_L g, \tag{2}$$

with the saturation energy E_L of the laser medium given by

$$E_L = \frac{h\nu_L}{2\sigma_L} A \tag{3}$$

(the factor 2 results from the double pass in the standing-wave cavity). If a Q-switched pulse reduces the gain by

$$\Delta g = g_i - g_f \tag{4}$$

($g_{i,f}$ are the intensity gain coefficient just before and that just after the pulse), it releases the energy $E_{\text{released}} = E_L \Delta g$ according to Eq. (2). The output energy is obtained from E_{released} by multiplication with the output coupling efficiency:

$$E_p = E_L \Delta g \frac{l_{\text{out}}}{l_{\text{out}} + l_p} \leq E_L g_i . \tag{5}$$

As Δg cannot exceed g_i, the quantity $E_L g_i$ represents an upper limit for the attainable pulse energy.

Δg, the only unknown quantity in Eq. (5), could be obtained by solution of rate equations (see Appendix A), but simple and useful equations can also be derived as follows. The pulse cycle consists of four different phases (see Fig. 2):

Phase 1

The absorber is in its unbleached state. A pulse can start to develop as soon as the pump has lifted the gain to the unsaturated value of the losses:

$$g_i = l + q_0 . \tag{6}$$

Now the intracavity power P grows slowly, starting from spontaneous-emission noise, until the intensity is sufficient to bleach the absorber. This point is reached long before the power has reached the maximum value because the saturation energy of the SESAM is typically chosen to be at least 1 order of magnitude less than the pulse energy. In addition, the absorber recovery time is normally at least as long as the pulse duration, so the absorber has little influence on the further evolution of the pulse.

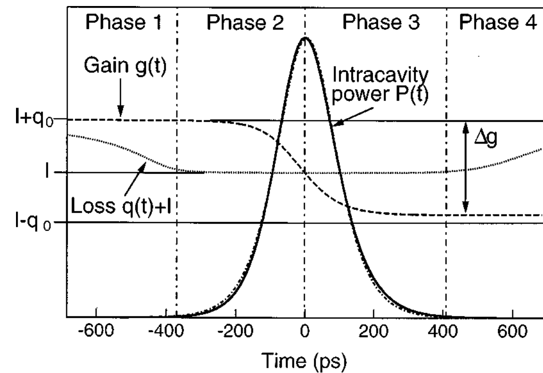

Fig. 2. Evolution of power, loss, and gain on the time scale of the pulse width obtained from numerical integration of the rate equations (Appendix A). As soon as the gain exceeds the loss, the power grows. The peak of the Q-switched pulse is reached when the gain equals the total losses. The parameters used are taken for a 200-μm-thick Nd:YVO_4 crystal and are as follows: $T_R = 2.61$ ps, $l = 14\%$, $\tau_L = 50\,\mu$s, $F_L = 37.3$ mJ/cm^2, $\tau_A = 200$ ps, $F_A = 40\,\mu$J/cm^2, pump parameter $r = 3$, $q_0 = 5\%$, and $A = (35\,\mu\text{m})^2\pi$.

Phase 2
As soon as the SESAM is fully bleached ($q = 0$), the power grows much more quickly [because the net gain is now $g_i - l - q \approx q_0$ with Eq. (6) and $q = 0$] until the gain starts to be depleted. The pulse maximum is reached when the net gain is zero, i.e., $g = l$.

Phase 3
With further depletion of the gain, the net gain becomes negative, and the intracavity power decays. Nevertheless the pulse still extracts significant energy in this phase.

Phase 4
After the pulse the absorber recovers, and the gain has to be pumped to the threshold level again before phase 1 of the subsequent pulse cycle can start. This takes much longer than the absorber recovery time τ_A. Therefore the absorber is fully recovered by the beginning of phase 1 [Eq. 6]. The time between two pulses is also much longer than the pulse width τ_p (see Fig. 3). Typical values in our experiments (see Section 3 below) are of the order of $\tau_A = 200\,\text{ps}$, $\tau_p = 100\,\text{ps}$, and $1/f_{\text{rep}} = 10\,\mu\text{s}$.

The gain reduction Δg in phase 3 depends on q_0 and l. The exact dependence can be calculated from rate equations, as is done in Appendix A; the results are shown in Fig. 4. In most practical cases we operate in the regime $q_0 \approx l$, where the pulse energy is optimized and also the pulses are nearly symmetric (see Subsection 2.B below). For $l \geqslant q_0$ we have (Fig. 4)

$$\Delta g \approx 2q_0. \tag{7}$$

Even for $q_0 = l$, expression (7) holds with ~20% accuracy. Inserting expression (7) into Eq. (5), we obtain a simple expression for the pulse energy:

$$E_p \approx \frac{h\nu_L}{2\sigma_L} A 2q_0 \frac{l_{\text{out}}}{l_{\text{out}} + l_p}, \qquad q_0 \leqslant l. \tag{8}$$

We can increase Δg and thus the pulse energy by increasing q_0 and l (Fig. 4). However, the available gain limits the value of $g_i = l + q_0$. In addition, we have to take into account that the parasitic losses introduced by the SESAM are typically proportional to the modulation depth. In Fig. 5 we have plotted the normalized output pulse energy versus l for different proportionality factors and initial gains (Appendix A). As long as there are parasitic losses, optimized pulse energy is achieved for values of l close to $l \approx q_0$, and expressions (7) and (8) can be applied.

C. Pulse Duration

As the saturation energy of the absorber is typically chosen to be small compared with the pulse energy, phase 1 has only a little influence on the pulse width, i.e., on the FWHM. For a rough estimate we assume that the gain during phase 2 remains undepleted at the value g_i [Eq. (6)], whereas the absorber is fully bleached ($q = 0$); this results in a net gain of $g_i - l - q \approx q_0$. With Eqs. (4) and (6) and expression (7) the net gain during phase 3 becomes $g_f - l - g = -\Delta g + g_i - l - q \approx -q_0$, as the absorber is still fully saturated ($q = 0$). Therefore the growth rate and the decay rate of the Q-switched pulse are both q_0/T_R (T_R is the cavity round-trip time), which would result in an estimated FWHM pulse duration of $2 \ln 2 T_R/q_0$. The exact result for the pulse width, with the decrease in growth and decay of the pulse during

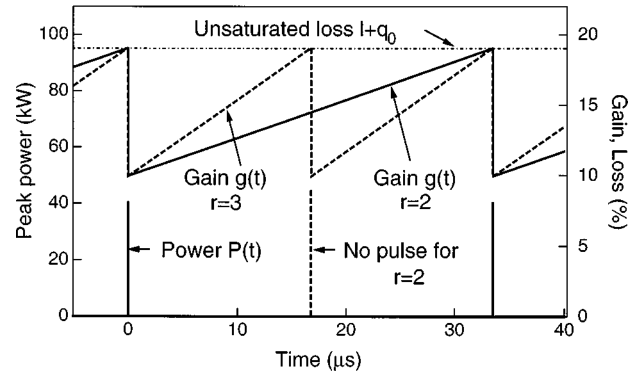

Fig. 3. Evolution of power, loss, and gain on the time scale of the repetition period for $r = 2$ and $r = 3$ obtained from a numerical integration of the rate equations (Appendix A). As soon as the gain reaches the unsaturated loss level a pulse is emitted and the gain is reduced by Δg. The next pulse is emitted when the pump has replaced the extracted energy. The repetition rate is proportional to $r - 1$. Besides r the simulation parameters are the same as in Fig. 2.

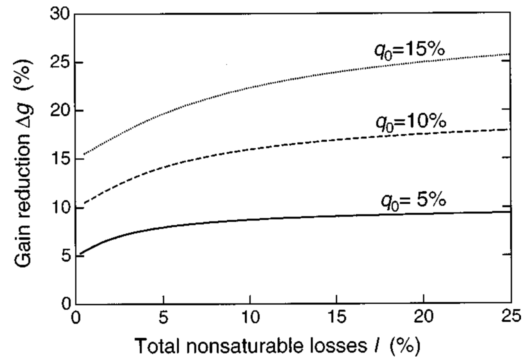

Fig. 4. Dependence of gain reduction Δg on the total nonsaturable losses obtained from the rate equations (Appendix A). For $l \geqslant q_0$ the approximation $\Delta g \approx 2q_0$ holds with at least 20% accuracy.

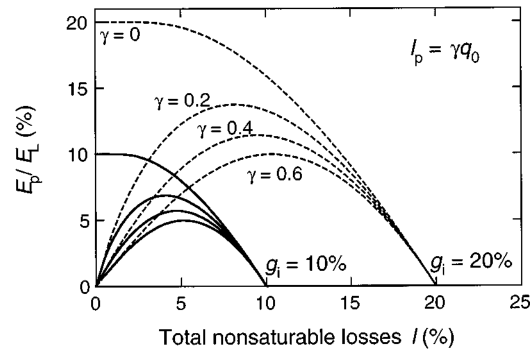

Fig. 5. Output pulse energy normalized to the saturation energy of the gain medium versus the total nonsaturable losses, for parasitic losses $l_p = \gamma q_0$ and two different fixed initial gains, obtained from the rate equations (Appendix A). Solid curves, the same values of γ in the same order as for the dashed curves. As soon as there are nonvanishing parasitic losses, maximum pulse energy is achieved for values of l close to $l \approx q_0 \approx g_i/2$.

saturation of the gain taken into account, contains another factor of ~2, as was noted earlier by Zayhowski and Kelley[18]:

$$\tau_p \approx \frac{3.52 T_R}{q_0}. \tag{9}$$

D. Pulse Shape

Figure 2 shows the result of a numerical simulation for the intracavity power of a Q-switched pulse together with an ideal sech^2 fit, confirming that the pulses are symmetric in the regime of interest ($l \geqslant q_0$) and that the sech^2 function appears to fit the simulated pulse very well. For $l < q_0$ the pulses become asymmetric.

E. Repetition Rate

To obtain the repetition rate f_{rep} we divide the average output power by the output pulse energy. The average power is given by $P_{\mathrm{av}} = \eta_s(P_P - P_{P,\mathrm{th}})$, where P_P is the pump power, $P_{P,\mathrm{th}}$ is the threshold pump power, and η_s is the slope efficiency, which is the product of the quantum efficiency, the pump efficiency, and the output-coupling efficiency. The result is

$$f_{\mathrm{rep}} = \frac{\eta_s(P_P - P_{P,\mathrm{th}})}{E_p} \propto r - 1. \tag{10}$$

Here $r = P_P/P_{P,\mathrm{th}}$ is the pump parameter. In the numerically obtained curves in Fig. 3 the $r - 1$ dependence of the repetition rate is clearly seen: The repetition rate for $r = 3$ is twice as large as for $r = 2$.

To write relation (10) in another useful form we connect the pump power and the threshold pump power to the small-signal gain coefficient g_0 and the loss coefficient:

$$P_P = \frac{h\nu_P A}{2\sigma_L \tau_L \eta_P} g_0, \qquad P_{P,\mathrm{th}} = \frac{h\nu_P A}{2\sigma_L \tau_L \eta_P}(l + q_0). \tag{11}$$

Here $h\nu_P$ is the pump photon energy, η_P is the pumping efficiency (i.e., the number of pump photons required on average for exciting one ion), and τ_L is the upper-state lifetime of the gain medium. We can derive Eqs. (11) by expressing the small-signal gain by the small-signal excitation density N_{20}, $g_0 = 2\sigma_L N_{20} L_g$, and using the fact that the decay rate that is due to spontaneous emission, $AL_g N_{20}/\tau_L$, has to be compensated for by the pump rate $\eta_P P_P/(h\nu_P)$. Inserting Eq. (5) and Eqs. (11) into relation (10) and using $\Delta g \approx 2q_0$ [relation (7)], we arrive at

$$f_{\mathrm{rep}} = \frac{g_0 - (l + q_0)}{\Delta g \tau_L} \approx \frac{g_0 - (l + q_0)}{2q_0 \tau_L}. \tag{12}$$

Equation (12) might be more appropriate for daily use, as the quantities can be estimated more easily. Note, however, that g_0 is proportional to τ_L, so a change in τ_L has little influence on f_{rep} far above threshold ($g_0 \gg l + q_0$). In addition, far above threshold we can neglect the term $l + q_0$ in Eq. (12), which then reduces to Eq. (2) of Ref. 7.

F. Remarks on Three-Level Lasers

So far we have considered only four-level lasers. With a few changes we can generalize the results of this section to three-level lasers. Here we have ground-state absorption in an unpumped crystal, and the gain coefficient per round trip is

$$g = 2(\sigma_L N_2 - \sigma_L{}^{\mathrm{abs}} N_1) L_g, \tag{13}$$

where $\sigma_L{}^{\mathrm{abs}}$ is the absorption cross section of the three-level gain medium at the laser wavelength and N_1 is the density of ions in the ground state. Assuming that all the ions are in either level one or level two for most of the time, we can write $N_1 = N_D - N_2$, where N_D is the dopant density. We obtain

$$g = 2(\sigma_L + \sigma_L{}^{\mathrm{abs}}) N_2 L_g - l_g, \tag{14}$$

where $l_g = 2\sigma_L{}^{\mathrm{abs}} N_D L_g$ is the loss coefficient per round trip caused by ground-state absorption. With Eqs. (1) and (14) the expression for the stored energy in a three-level laser medium is

$$E_{\mathrm{stored}} = \frac{h\nu_L}{2(\sigma_L + \sigma_L{}^{\mathrm{abs}})} A(g + l_g) = E_L(g + l_g), \tag{15}$$

with the modified expression for the saturation energy of the gain medium:

$$E_L = \frac{h\nu}{2(\sigma_L + \sigma_L{}^{\mathrm{abs}})} A. \tag{16}$$

With these modifications we can still use expressions (4)–(12) [except expression (8) and Eqs. (11)], i.e., the expressions for gain reduction Δg, pulse energies E_{released} and E_p, pulse duration τ_p, and repetition rate f_{rep}.

We see that the main effect of the ground-state absorption is to reduce saturation energy E_L and thus pulse energy E_p, although we note that the typical tendency of three-level lasers to operate at longer wavelengths (where the reabsorption is weaker) could in practice even increase the pulse energy, particularly in the case of high dopant concentrations.

3. EXPERIMENTS

A. Semiconductor Saturable-Absorber Mirror

The use of a semiconductor saturable absorber (rather than, e.g., a doped crystal) as a passive Q switch in a microchip laser is advantageous for several reasons: First, the SESAM[2,3] is used as an end mirror and has an effective penetration depth of only a few micrometers. Thus we can add a saturable absorber to the microchip laser with only a negligible increase in the cavity length. Therefore we maintain a shorter cavity length and obtain shorter Q-switched pulse widths [expression (9)] than with other approaches that require larger bulk modulation elements.[22] Second, the bandgap of the absorber layer can be adapted to the laser wavelength. It is therefore possible to adapt the system of the absorber to other laser materials at different lasing wavelengths,[8,9] in contrast to bulk absorbers such as Cr^{4+}:YAG, which are limited to specific spectral regions. And, finally, there is enough design freedom to permit independent adjustment of the saturation intensity

$$I_A = \frac{E_A}{A\tau_A} \tag{17}$$

and the saturable losses q_0 even if the mode size (on the absorber) is fixed. In microchip lasers the laser mode size, which is nearly constant over the whole length of the flat–flat cavity, cannot be changed over a wide range, because the transverse modes are determined mainly by the thermal lens and by thermal expansion and gain guiding[23,24] and the mode sizes in the laser medium and the absorber always are equal. The pulse width, the repetition rate, and the pulse energy are determined mainly by the modulation depth q_0 (Section 2), a parameter that we can vary over a wide range while keeping E_A and I_A small. Thus the pulse width as well as the repetition rate can be reliably varied over several orders of magnitude.

The SESAM consists of a semiconductor saturable-absorber layer grown upon a highly reflecting bottom mirror. For the microchip lasers it normally has a high-reflection coating for the pump wavelength at the top, which avoids heating of the SESAM by absorption of residual pump light and can increase the pump absorption efficiency. The same coating has a predesigned reflectivity for the laser wavelength to control the amount of the saturable absorption and the saturation intensity of the device. The thickness of the absorber layer is adjusted for antiresonance of the Fabry–Perot structure that is formed by the lower Bragg mirror and the dielectric top reflector. Operation in this regime helps to avoid significant temperature dependence and optical bistability.

The modulation depth ΔR of a SESAM is defined as the maximum reflectivity change of the absorber:

$$\Delta R = 1 - \exp(-q_0). \tag{18}$$

For $q_0 \ll 1$, Eq. (18) becomes $\Delta R \approx q_0$. Together with E_A and τ_A, ΔR is one of the most important experimental parameters of the SESAM. It is controlled mainly by the reflectivity of the top reflector and the number or thickness of the absorber layers. With the SESAM we always introduce nonsaturable losses into the cavity, which are typically proportional to ΔR but also depend on the growing parameters.

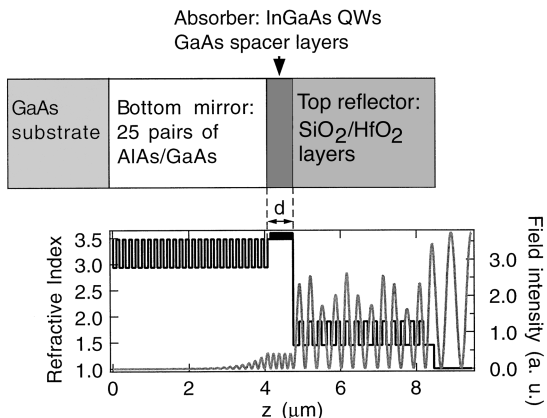

Fig. 6. Structure of a SESAM with a dielectric top reflector and the standing-wave intensity pattern in this structure. The effective penetration depth is of the order of only a few micrometers. QW's, quantum wells.

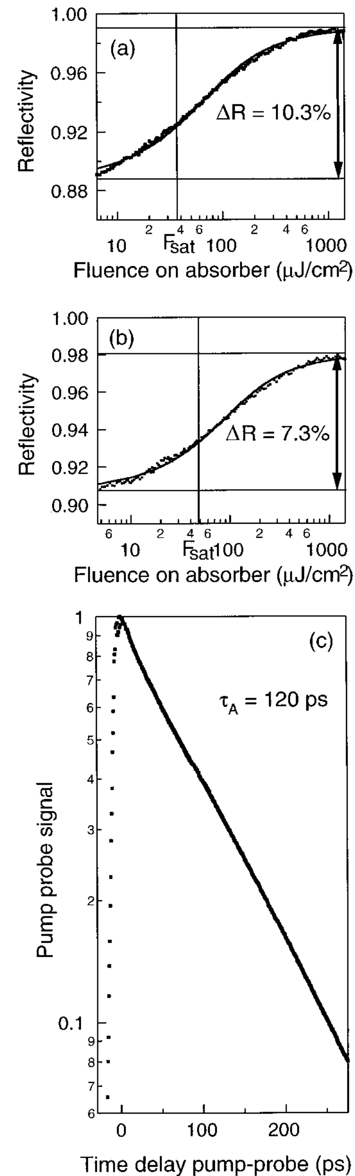

Fig. 7. Measured change in reflectivity versus incident pulse fluence (filled squares) and theoretical fit (solid curves) for a SESAM consisting of 18 quantum wells and (a) a 25% and (b) a 50% top reflector. The measured temporal pulse response is shown in (c) (filled squares) together with an exponential fit (solid curve).

1. 1-μm SESAM

For the 1-μm experiments described here, SiO_2/HfO_2 dielectric top reflectors with a reflectivity of 25% or 50% were used. The saturable absorbers were grown either by metal-organic chemical-vapor deposition (MOCVD) at normal growth temperature or by molecular-beam epitaxy (MBE) at temperatures below the normal growth temperature, namely, at 480 °C, to prevent surface striations owing to the lattice mismatch of GaAs and InGaAs. In addition, the MBE growth temperature influences τ_A and therefore I_A [Eq. (17)],[25] which helps to control q_0 and I_A independently. MOCVD growth and MBE growth at the temperature mentioned typically result in lifetimes of hundreds of picoseconds and therefore in small saturation intensities. Both designs consist of an $In_{0.25}Ga_{0.75}As/GaAs$ multi-quantum-well absorber grown

on top of a highly reflecting AlAs/GaAs Bragg mirror (25 pairs). The SESAM design and the resultant standing-wave pattern in the absorber are shown in Fig. 6. Because InGaAs with a bandgap of 1 μm is not lattice matched to GaAs, there is a critical thickness for the absorber layer above which cross hatches that are due to strain significantly degrade the surface quality.[26] This critical thickness is generally larger for MBE growth at low to intermediate temperatures but at the expense of a smaller modulation depth and higher nonsaturable losses.[25]

Figure 7 shows the measured change in reflectivity versus incident pulse fluence and the temporal pulse response together with theoretical fits of two of the SESAM's used for the experiments described in Subsection 3.C below. For these measurements we used a mode-locked Nd:YVO_4 laser that produced 7-ps pulses at a repetition rate of 100 MHz and a wavelength of 1064 nm. The same MOCVD-grown absorber with 18 quantum wells was coated with two different top reflectors for the lasing wavelength. The SESAM coated with a 25% reflector has a modulation depth $\Delta R = 10.3\%$ and a saturation fluence $F_A = 36\ \mu J/cm^2$ [Fig. 7(a)]. The SESAM with a 50% top reflector has $\Delta R = 7.3\%$ and $F_A = 47\ \mu J/cm^2$ [Fig. 7(b)]. The absorber lifetime was $\tau_A = 120$ ps [Fig. 7(c)], independently of the top reflector but depending on the excitation density.

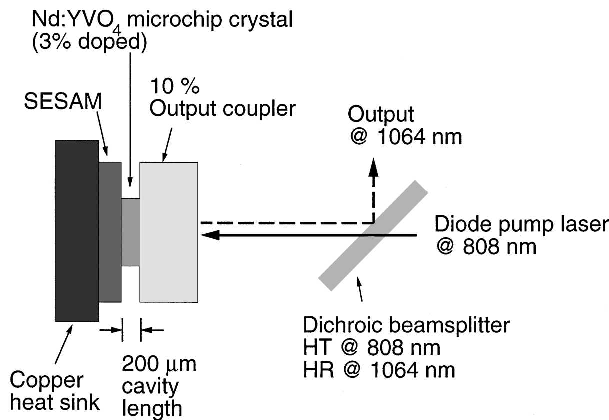

Fig. 8. Schematic of the *Q*-switched Nd:YVO_4 microchip laser with a SESAM in direct contact with the crystal. The microchip cavity is pumped through a dichroic beam splitter, which transmits the pump beam at 808 nm and reflects the output beam at 1064 nm. HR, highly reflecting; HT, highly transmitting.

2. 1.5-μm SESAM

The SESAM's for the eye-safe microchip laser were grown by MOCVD. They consist of a bulk $In_{0.58}Ga_{0.42}As_{0.9}P_{0.1}$ absorber and an InP cap layer grown upon a bottom mirror formed from 40 pairs of $In_{0.65}Ga_{0.35}As_{0.73}P_{0.27}$/InP layers. The dielectric SiO_2/HfO_2 top coating had a designed reflectivity of 50% or 70% at laser wavelength of 1.53 μm and high reflectivity at the pump wavelength of 975 nm.

B. Experimental Setup

The experimental setup for the 1-μm experiments is shown in Fig. 8. The microchip crystal was sandwiched between an output coupler and a SESAM. The top reflector of the SESAM was a high reflector for the pump wavelength and a partial reflector for the lasing wavelength. The crystal was pumped by a 2-W, 200-μm-stripe-size broad-area emitter diode through a dichroic beam splitter that transmits the pump light and reflects the output beam. The diode pump laser was focused down to radii of 20 and 50 μm inside the microchip crystal for the fast and the slow axes, respectively. The pump wavelength was 808 nm. The microchip crystals that we used in the 1-μm experiments were either Nd:YVO_4 or Nd:$LaSc_3(BO_3)_4$ (Nd:LSB) crystals of different thicknesses.

The setup for the 1.5-μm eye-safe microchip laser is similar to the one shown in Fig. 8. We used a 1-mm thick Er:Yb:glass disk pumped by a Ti:sapphire laser, although diode-pumped operation has also been demonstrated.[9] The main material properties of several gain media are summarized in Table 1.

Table 1. Comparison of Material Properties of Nd:YVO_4, Nd:LSB, Nd:YAG, Yb:YAG, and Er:Yb:Glass[a]

Parameter emission wavelength (nm)	Type of Laser Material				
	Nd:YVO_4 1064	Nd:LSB 1062	Nd:YAG 1064	Yb:YAG 1030	Er:Yb:glass[b] 1535
Doping D	≤3%	≤100%	~1.1%	20%	Er, $7.3 \times 10^{19}\ cm^{-3}$; Yb, $1.8 \times 10^{21}\ cm^{-3}$
Absorption length	90 μm ($D = 3\%$)	110 μm ($D = 25\%$)	1.2 mm	650 μm	600 μm
Absorption bandwidth (nm)	1.5	3.0	0.8	≈30	0.8
Gain bandwidth (nm)	1.0	4.0	0.5	≈8.5	37
Upper-state lifetime (μs)	50 ($D = 3\%$)	87 ($D = 25\%$)	250	950	7900
Gain cross section ($\times 10^{-19}\ cm^2$)	25	1.3	3.3	0.25	0.08
Absorption cross section ($\times 10^{-19}\ cm^2$)	2.7	0.71	1.5	0.056	0.021
Saturation fluence F_L (mJ/cm^2)	37.3	720	333	≈3900	≈8090
Thermal conductivity (300 K; W/cm K)	0.052	0.028	0.13	0.13	0.0085
dn/dT ($\times 10^{-6}$ K)	3	4.4	7.3	7.3	−1
Refractive index	1.96	1.82	1.84	1.84	1.52
m	0.31	1.42	1.95	19	26.3

[a] The data are taken from Refs. 27–33.
[b] QX/Er; Kigre, Inc.

Table 2. Overview of Results Achieved with Several SESAM's and Microchip Crystals[a]

Gain	ΔR (%)	P_P	P_{av} (mW)	P_{peak}	τ_p	E_p	f_{rep}	Ref.
Nd:YVO_4, 185 μm	13	460 mW	8.5	1.4 kW	37 ps	53 nJ	160 kHz	
Nd:YVO_4, 200 μm	13	460 mW	5.3	1.1 kW	56 ps	62 nJ	85 kHz	7
Nd:YVO_4, 200 μm	10	940 mW	58	5.4 kW	68 ps	0.37 μJ	160 kHz	7
Nd:YVO_4, 200 μm	6	570 mW	82	1.4 kW	117 ps	0.16 μJ	510 kHz	
Nd:YVO_4, 440 μm	13	1.1 W	120	1.6 kW	181 ps	0.28 μJ	440 kHz	
Nd:YVO_4, 440 μm	2.4	1.1 W	350	17 W	2.64 ns	45 nJ	7.8 MHz	
Nd:LSB, 220 μm	2.4	450 mW	51	1.6 kW	360 ps	0.59 μJ	86 kHz	34
Er:Yb:glass, 1 mm	1.1	744 mW	1.3	725 W	5.6 ns	4 μJ	320 Hz	9

[a] Refs. 7, 9, and 34.

C. *Q*-Switching Results

Before going into detail, we refer to Table 2, which is meant to give an overview of what kind of performance is achieved from the microchip lasers passively *Q*-switched with a SESAM. We achieved the shortest pulses with a MBE-grown SESAM (growth temperature $T = 480\,°\mathrm{C}$) with 35 InGaAs quantum wells, a 50% top reflector, and an uncoated 185-μm-thick Nd:YVO_4 crystal. With a 10% output coupler and an incident pump power of 460 mW we obtained single-frequency *Q*-switched pulses of 37-ps FWHM (Fig. 1) and a peak power of 1.4 kW. The oscillations after the pulse are detector ringing, which is identified by the comparison of the trace with the impulse response of the detecting system. The average output power was 8.5 mW, the repetition rate was 160 kHz, and the pulse energy was 53 nJ. In this case the modulation depth of the saturable absorber was approximately 13%. To our knowledge, these are the shortest *Q*-switched pulses ever generated with a solid-state laser. From expression (9) we get with these parameters a pulse width of 64 ps. This deviation can be explained by the Fabry–Perot effect of the air gap between SESAM and crystal, which can enhance the coupling into the SESAM and therefore the modulation depth.

We achieved peak powers of as much as 5.4 kW and repetition rates of 27 kHz–7 MHz simply by using different SESAM's, different pump powers, and Nd-doped crystals of different thicknesses. We obtained pulse energies of as much as 4 μJ with Er:Yb-doped glass at 1.5 μm.[9]

The pulse widths were measured with a 50-GHz sampling oscilloscope and a 45-GHz p–i–n photodetector. The time resolution was better than 15 ps, confirmed with 150-fs pulses from a mode-locked Nd:glass laser. Because of the microsecond pulse-to-pulse timing jitter, the oscilloscope had to be triggered on each pulse itself (rather than on the preceding pulse) to preserve the time resolution. We used a 10-m optical delay line for the signal, which provided the required delay after the trigger signal.

In what follows, we first present measurements for lasers with Nd:YVO_4 as the gain material at a wavelength of 1.064 μm. Then, at the end of this section we show experiments done with an eye-safe Er:Yb:glass microchip laser. The parameters of these gain materials (cross sections, thermal properties, emission bandwidth, etc.) and the operation parameters vary widely, but our model describes both kinds of laser with good accuracy (pulse duration, pulse fluence, etc.).

Figures 9–12 show data from experiments with a 435-μm-thick Nd:YVO_4 crystal as the gain medium. The crystal was antireflection (AR) coated on both sides to avoid etalon effects between crystal and output coupler or crystal and SESAM. This was necessary so we could be sure of the exact value of output coupling and the coupling into the SESAM, because changing the absorber could result in varying air gaps of different thicknesses (and therefore in different etalon effects) between the crystal and neighboring elements.

The average output power, repetition rate, emission wavelength, effective laser area in the cavity, and the pulse width were measured simultaneously as a function of pump power for different SESAM's and different output couplers. The pulse energy was determined from the average output power and the repetition rate; the fluence, from the pulse energy and the effective area. The effective mode area in the laser was calculated from beam size measurements outside the laser, monitored with a beam profiler. The emission wavelength was measured because it determines the effective emission cross section: One cannot always be sure to have oscillation at the maximum emission cross section because the mode spacing is of the order of the gain bandwidth, as a result of the short cavity length. In the experiments depicted in Figs. 9–11 the laser operated near the maximum of the gain curve, resulting in a saturation energy of $E_L = 37.3$ mJ/cm^2.

Figure 9 shows the pulse width, the repetition rate, and the fluence versus pump power for two SESAM's with different modulation depths ΔR (Fig. 7). The same MOCVD-grown absorber with 18 quantum wells was used with top reflectors of 25% and 50%, resulting in modulation depths of 10.3% and 7.3%, respectively. The dashed curves correspond to the SESAM with $\Delta R = 7.3\%$; the solid curves, to the SESAM with $\Delta R = 10.3\%$. In both cases the output coupling was 9%. The absorber lifetime was $\tau_A = 120$ ps [Fig. 7(c)], independently of the dielectric top reflector. The saturation fluences of the absorbers, $F_A = E_A/A$, were 36 and 47 μJ/cm^2, respectively. This means that for typical mode areas of $\sim$4000 μm^2 the absorber is already cw saturated at 12 and 16 W, respectively [Eq. 17], i.e., at power levels far below the typical peak powers of the pulses of several hundreds of watts (phase 1; Subsection 2.B). The parasitic losses l_p (calculated from the slope efficiencies) were 3% for the setup with the larger modulation depth and 2% for the one with $\Delta R = 7.3\%$.

The pulse width in Fig. 9 appears to be nearly independent of pump power, as expected, and fits the theoretical value within 20% [thin straight lines; expression (9)]. With the exception of the first point close to the threshold, the fluence is nearly independent of the pump power. The general deviation of ~30% from the theoretical curve [expression (8)], observed in all measurements, can be due to the transverse effects and the spatial hole burning that were neglected in Section 2. For the same absorber we can vary the repetition rate by more than 1 order of magnitude by just varying the pump power without changing the pulse width and the fluence significantly.

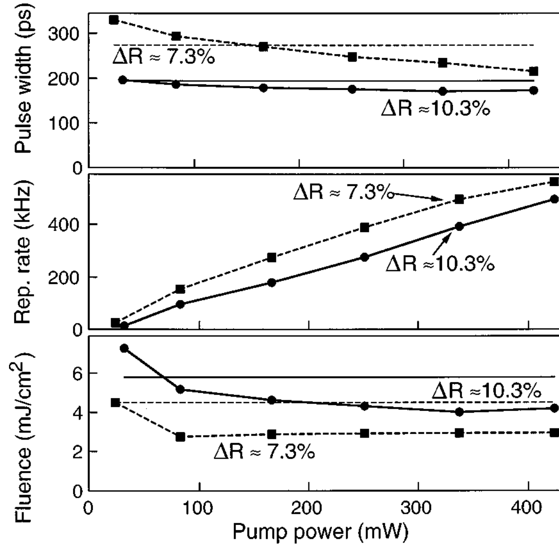

Fig. 9. Pulse width, repetition rate, and output pulse fluence as a function of the pump power for two different modulation depths. Thin horizontal lines, theoretical values that correspond to those shown by the solid and dashed curves. The experiments were carried out with a 435-μm-thick 3% doped Nd:YVO_4 crystal, AR coated on both sides, and a 9% output coupler. The parasitic losses l_p were 3% for the setup with the higher ΔR and 2% for the lower modulation.

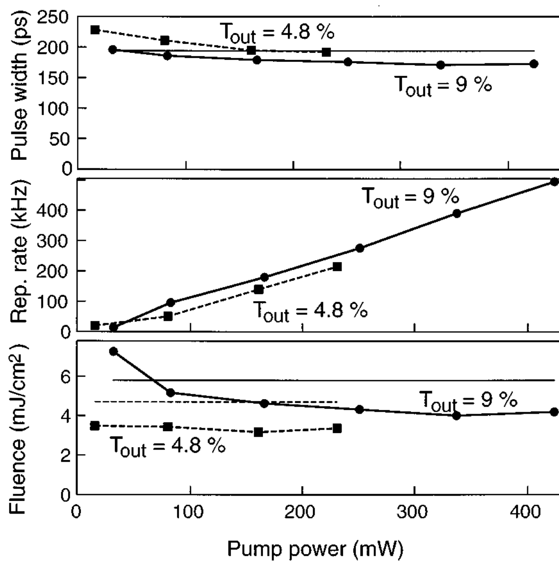

Fig. 10. Pulse width, repetition rate, and output pulse fluence as a function of the pump power for two different output couplers. Thin horizontal lines, theoretical values that correspond to those shown by the solid and dashed curves. The experiments were carried out with a 435-μm-thick 3% doped Nd:YVO_4 crystal, AR coated on both sides, and $\Delta R = 10.3\%$. The parasitic losses l_p were 3%.

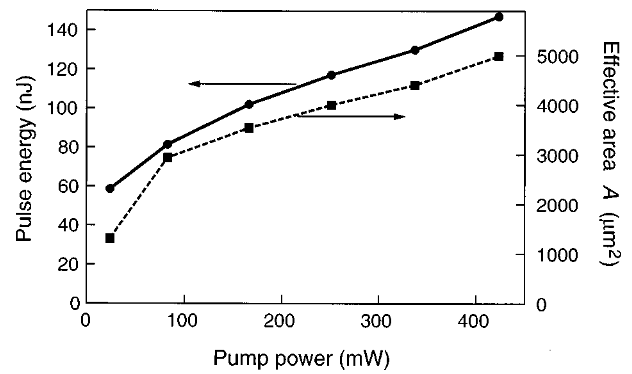

Fig. 11. Pulse energy and effective laser area as a function of the pump power. The measurement was carried out with a 435-μm thick 3% doped Nd:YVO_4 crystal, AR coated on both sides, $\Delta R = 7.3\%$, and $T_{\text{out}} = 9\%$. The pulse energy is strongly correlated with the effective area, resulting in a constant fluence $F = E_p/A$ (see Fig. 9).

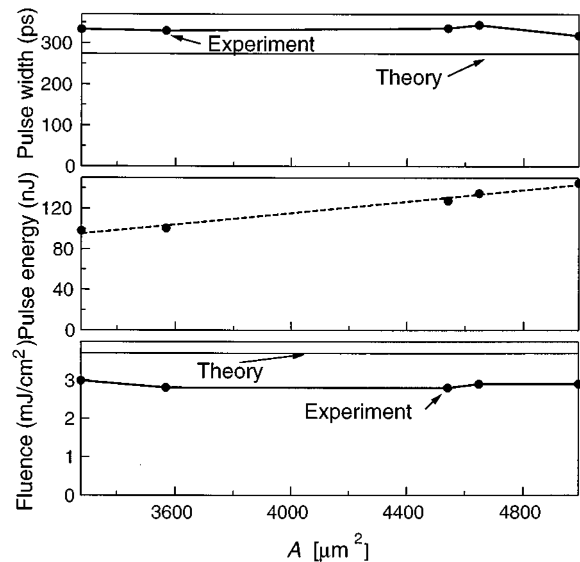

Fig. 12. Pulse width, pulse energy, and output pulse fluence as a function of the effective area, which we controlled by varying the pump spot size. The experiments were carried out with a 435-μm-thick 3% doped Nd:YVO_4 crystal, AR coated on both sides, and $\Delta R = 7.3\%$, $T_{\text{out}} = 4.2\%$. The pump power was held constant at 160 mW. $l_p = 2\%$. The dashed curve is a linear fit to the pulse energy, which appears to be directly proportional to the effective area, without any additive constant.

Figure 10 shows data similar to those in Fig. 9 but for different output couplers. The same SESAM as in Fig. 9 with $\Delta R = 10.3\%$ was used, with output couplers of 4.8% and 9%. The parasitic losses l_p were 3%. The pulse width is nearly independent of the output-coupler transmission and pump power and fits the theoretical curve well. For the larger T_{out} the output-coupling efficiency and thus the fluence are higher. Again the deviation of the measured fluence from the theory is systematically ~30%, for the same reasons as for Fig. 9.

In Figs. 9 and 10 we have shown fluence rather than pulse energy versus pump power, because the effective area of the laser mode changes significantly with pump

power as a result of variations in thermal conditions. Figure 11 shows the pulse energy and the effective area as a function of the pump power for laser parameters $\Delta R = 7.3\%$ and $T_{\text{out}} = 9\%$. The pulse energy changes by more than a factor of 3 because of an increase in mode area A, whereas fluence $F = E_{\text{out}}/A$ stays constant. Unlike in the research reported in Ref. 23, we have an increasing effective laser area with increasing pump power, which might be due to the different thermal properties: Our cavity (Fig. 8) has an asymmetric and an especially nontransverse heat flow. The SESAM has much better heat conductivity than the output coupler and the surrounding air. Therefore the main heat sink will be the SESAM, mounted upon a copper block. The only poorer heat conductor on the SESAM side is the dielectric coating. For example, we observed different pump-power dependencies of the effective area for different coating thicknesses and materials.

For Fig. 12 we varied effective area A while keeping all laser parameters constant ($T_{\text{out}} = 4.2\%$; $\Delta R = 7.3\%$). We changed A simply by moving the whole microchip laser out of the pump focus. The pump power was held constant at 160 mW. Thus the pumping intensity and therefore the pump parameter r, the inversion, and the average output power decreased with increasing A. As expected, this did not affect the pulse fluence and duration, whereas the pulse energy increased with the mode area and the repetition rate was reduced accordingly. The dashed curve in Fig. 12 is a linear fit (without an additional constant) for the pulse energy versus A, confirming the A dependence of expression (8).

To experimentally verify expression (9) we varied the cavity round-trip time T_R (Fig. 13). This was done in a slightly different, nonmonolithic cavity setup shown in the inset of Fig. 13. We used a curved output coupler ($T_{\text{out}} = 1\%$; radius of curvature, 10 cm) to ensure cavity stability even for longer cavity lengths without being obligated to change the crystal thickness and therefore many cavity parameters for every data point. The crystal, 200-μm-thick uncoated 3% doped Nd:YVO_4, was bonded to a SESAM consisting of nine quantum wells and no dielectric top reflector. We changed T_R by varying the length of the air gap between the output coupler and the crystal. The pulse width turned out to be directly proportional to the cavity length (Fig. 13). Changing the cavity length might slightly change the location of the spot on the SESAM; the bad data points in Fig. 13 can thus be explained as being due to inhomogeneities of the absorber. The modulation depth of the absorber can be determined with the help of the slope of the linear fit to the data points and expression (9). This calculated modulation depth is $\Delta R_{\text{cal}} \approx 4.5\%$, which is in excellent agreement with the modulation depth determined with the standard method mentioned in Subsection 3.A.1, giving $\Delta R = 4.3\%$.

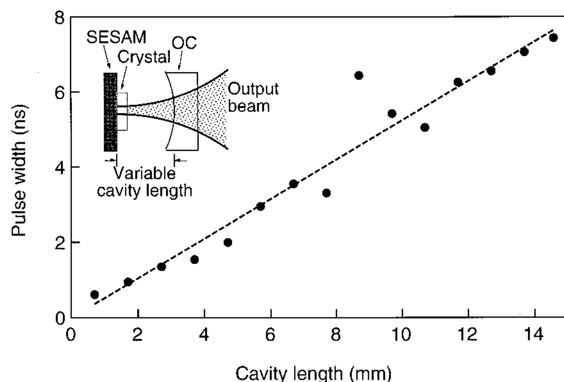

Fig. 13. Pulse width as a function of the cavity length, measured with a cavity as shown in the inset: A 200-μm-thick 3% doped Nd:YVO_4 crystal was bonded to an uncoated SESAM with an effective modulation depth $\Delta R \approx 4.3\%$. Resonator stability was ensured by a curved 1% output coupler (radius of curvature, 10 cm) also for large air gaps between crystal and output coupler. With the linear fit (dashed curve) and expression (9) the modulation depth was calculated to be $\Delta R_{\text{cal}} = 4.5\%$. OC, output coupler.

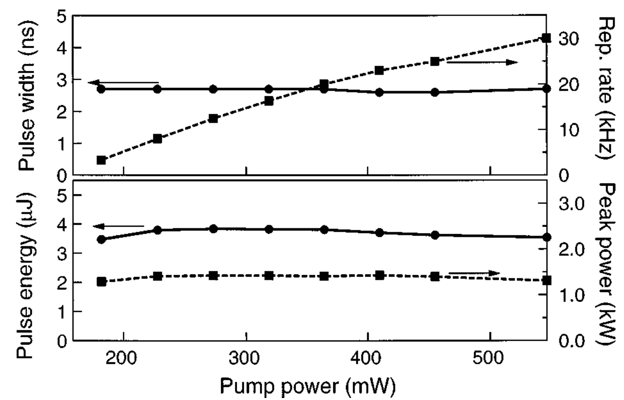

Fig. 14. Pulse width, repetition rate, pulse energy, and peak power as a function of the pump power of an eye-safe 1.5-μm microchip laser using 1-mm-thick Er:Yb:glass (Kigre Inc., QX/Er) as the gain medium; $\Delta R \approx 1.5\%$, $T_{\text{out}} = 5\%$. The parasitic losses l_p were estimated to be 1.5%. The pulse energy, the pulse width, and the peak power appear to be independent of the pump power.

To test the applicability of our model to lasers operating in a different parameter range we also carried out a number of experiments on Er:Yb:glass lasers with output at 1.5 μm. The quasi-three-level laser medium Er:Yb:glass[35] has a broad emission spectrum, enhancing the tendency for multiple longitudinal mode oscillation and small emission cross-sections, which result in higher pump thresholds, lower small-signal gain, and larger pulse fluences (even close to the damage threshold of the SESAM) than Nd-doped crystals. The thermal characteristics differ significantly from those of Nd:YVO_4; namely, the heat conductivity is relatively poor and the refractive index falls with rising temperature, resulting in a negative thermal lens induced by the pump. The cavity mode is therefore stabilized mainly by gain guiding and thermal expansion.

Figure 14 shows pulse width, repetition rate, pulse energy, and peak power for the 1.5-μm Er:Yb:glass microchip laser (as already described in Ref. 9). A 1-mm thick Er:Yb:glass disk (Kigre, Inc., QX/Er) was used, pumped by a Ti:sapphire laser with a beam radius of 50 μm. From the measured pulse width of 2.7 ns we calculated that the effective modulation depth ΔR (which was influenced by Fabry–Perot effects at the interfaces) was 1.2%; the parasitic losses were 1.5%, and the output coupling was 5%. As expected, the pulse width shows no pump-

power dependence (Fig. 14). In contrast to the results for the $Nd:YVO_4$ lasers, here the pulse energy was also independent of the pump power. This observation is compatible with the assumption of constant pulse fluence (as predicted by the model) and constant mode area. The latter was not measured but can be expected to be smaller than the pump mode area and not to increase considerably with pump power, as for a three-level gain medium it is limited by reabsorption in the wings of the transverse mode profile. The measured pulse energy of 4 μJ is compatible with the assumption that A is one third of the pump area and the laser parameters are as given above. Thus also for the Er:Yb:glass laser the experiments are in reasonable agreement with the theory. Again we can vary the repetition rate over a wide range without changing the pulse width and energy, just by changing the pump power.

4. DESIGN GUIDELINES

As we have seen that the model describes the performance of microchip lasers with reasonable accuracy, we now apply the theoretical results to derive practical guidelines for the design of such lasers.

First we address some general requirements. Stable passive Q switching requires the modulation depth of the absorber to be large enough. More precisely, the decay rate of intensity fluctuations must exceed the relaxation rate of the gain; the condition for Q switching is[36,37]

$$-\frac{1}{T_R}\, I\, \frac{\mathrm{d}q}{\mathrm{d}I}\bigg|_{\text{cw steady state}} > \frac{r}{\tau_L}\bigg|_{\text{cw steady state}}. \tag{19}$$

Here τ_L is the upper-state lifetime of the gain medium. Our experience is that Q switching is easily achieved in microchip lasers, except for SESAM's with very small modulation depths (smaller than ~3% for Nd doped gain materials).

An obvious but important criterion for solution of various design problems is that the gain be sufficient to reach the laser threshold. The steady-state small-signal gain $g_0 = 2\sigma_L N_{20} L_g$ [or Eq. (13) for three-level lasers] has to exceed the initial gain g_i given by Eq. (6) to start laser oscillation and Q switching. But, for a given g_0, g_0 obviously presents an upper limit for g_i and thus for the gain reduction Δg.

The cavity round-trip time is related to the length of the gain medium by $T_R = 2nL_g/c$, where c is the speed of light in vacuum and n is the refractive index of the gain material. L_g is usually chosen to be of the order of the absorption length L_{abs}, which depends on the doping level. For L_g much larger than L_{abs} one increases the pulse width without any other benefit, whereas a smaller L_g will compromise the laser efficiency. The requirement of generating sufficient gain ($g_0 > g_i$) finally leads to the condition that

$$\frac{\sigma_L N_D c}{2n} > \frac{l + \Delta R}{T_R}, \tag{20}$$

which permits a pump parameter of $r = 2$ to be reached for full inversion, meaning that the small-signal excitation density N_{20} equals the dopant density N_D (we assume that sufficient pump power is available). This gain criterion will be an ultimate limit for the following design guidelines.

The beam quality of the pump laser is usually not a critical parameter for a microchip laser because of the short cavity length. In addition, a circular output beam profile is easily achieved, even with an elliptical pump spot. In the following subsections we discuss how various design objectives can be achieved.

A. Single-Longitudinal-Mode Operation

Q-switched operation can occur in a single- or in multiple-longitudinal cavity modes. The latter case is less attractive because it leads to mode-beating effects and increased timing jitter. The microchip approach is advantageous for single-mode operation because of the large mode spacing, which is caused by the short cavity length. A figure of merit for laser materials with respect to single-mode operation is the parameter m, defined in Ref. 38 as the number of axial modes within the gain bandwidth, assuming a microchip cavity length L_g equal to the absorption length $L_{\text{abs}} = 1/\alpha$ of the laser material:

$$m = \frac{\Delta f_g}{\left(\dfrac{c}{2nL_g}\right)} = \frac{2n\Delta f_g}{\alpha c}. \tag{21}$$

Here Δf_g is the FWHM gain bandwidth and α is the absorption coefficient. As can be seen from Table 1, $Nd:YVO_4$ has a particularly low (and thus favorable) value of m, which is 4.6 times smaller than for Nd:LSB, 6.3 times smaller than for Nd:YAG, and 85 times smaller than for Er:Yb:glass. Generally glasses as host materials have larger m values because of their broader emission spectra. Note, however, that the use of a suitable intracavity filter can ensure single-mode operation even for materials with high m values.[39] For example, single-mode operation was achieved in a Er:Yb:glass laser by incorporation of piece of $LiNbO_3$, which in conjunction with the output coupler formed a Fabry–Perot structure.[9]

B. Short Pulses

We have seen [expression (9)] that the pulse duration (for $\Delta R \approx q_0$) is given by

$$\tau_p \approx \frac{3.52 T_R}{\Delta R}. \tag{22}$$

For small τ_p we obviously need a large modulation depth and a short round-trip time. Here we are ultimately limited by the gain criterion [inequality (20)]. The round-trip time is related to the absorption length L_{abs} and thus is limited for a given gain medium by the maximum possible doping level. Reducing L_g below L_{abs} is possible but compromises the efficiency of the laser and is not useful anyway if the reduced gain would require a smaller value of ΔR. The use of a high-gain material (with large σ_L and a large possible doping level) is favorable for short-pulse generation; the gain bandwidth is not a limiting factor, even for high-gain materials. In particular, $Nd:YVO_4$ with its small possible absorption length [90 μm (Ref. 31)] and large σ_L is well suited for this purpose. In addition, the narrow emission bandwidth results in a

small m parameter, so single-mode operation is achieved even at high output powers, finally limited by spatial hole burning.[20,21]

The SESAM that we produced with good optical quality had a maximum modulation depth ΔR of approximately 13% (at 1-μm laser wavelength), limited by cross hatches that are due to strain in the absorber (see Subsection 3.A.1). The limitations of the crystal thickness imposed by the absorption length, the gain criterion, and the polishing technique lead to L_g of the order of 100 μm (for Nd:YVO_4). The shortest Q-switched pulses of 37-ps duration (see Fig. 1) were obtained from a 185-μm-long Nd:YVO_4 crystal.

C. Large Pulse Energy

To achieve large pulse energies (for $\Delta R \approx q_0$) of

$$E_p = \frac{h\nu_L}{2\sigma_L} A 2\Delta R \frac{l_{\text{out}}}{l_{\text{out}} + l_p}, \tag{23}$$

we need large modulation depth, laser mode area, and output coupling efficiency as well as a small emission cross section. A large laser mode area can be achieved with a large pump spot but is limited by transverse mode instabilities and a large threshold power. The main requirement for achieving large pulse energies is choice of a gain material with a small gain cross section, which results in a large saturation energy. Therefore, in the 1-μm-region, Yb:YAG with its small gain cross section should allow for higher pulse energies than Nd-doped crystals do. On the other hand, the limiting factor might be the damage fluence of the SESAM, which is of the order of 30 mJ/cm^2 for a SESAM with a top reflector of ~30% (see Subsection 3.A) and pulse durations of ~30 ps. The damage threshold can be higher for higher top reflectors. It scales with the ξ factor [Eq. (13) of Ref. 25], which is the ratio of the peak intensity inside the Fabry–Perot structure of the SESAM and outside it. The damage fluence also scales with $\tau_p^{1/2}$ for pulse durations above ~30 ps.[40]

As we stated in Subsection 2.B and showed in Fig. 5, maximum pulse energy is obtained for values of l close to $q_0 \approx \Delta R$ if the nonsaturable losses of the SESAM are accounted for. Then Eq. (23) reduces to $E_p \approx 2E_L l_{\text{out}}$. But still g_0 has to exceed g_i, and therefore ΔR cannot be larger than $g_0/2$.

Generally, another way to increase the pulse energy by using a smaller gain cross section would be to apply an intracavity filter that enforces operation at a wavelength away from the gain maximum, or even at a different transition. This was done in the research reported in Ref. 8, forcing a Nd:YVO_4 laser to oscillate on the 1.34-μm line (where σ_L is smaller than at 1 μm) but still benefiting from the good thermal and crystal properties.

D. Large Peak Power

For some applications it is interesting to have a large peak power P_{peak}, given (for $\Delta R \approx q_0$) by

$$P_{\text{peak}} = S_p \frac{E_p}{\tau_p} \propto \frac{(\Delta R)^2 A}{T_R \sigma_L} \eta_{\text{OC}}. \tag{24}$$

Here S_p is the pulse shape factor ($S_p = 0.88$ for sech^2 pulses) and $\eta_{\text{OC}} = l_{\text{out}}/(l_{\text{out}} + l_p)$ is the output-coupling efficiency. A large modulation depth is obviously important. Equation (24) also suggests use of a small round-trip time T_R, but this is beneficial only as long as enough gain can be generated to allow for a large modulation depth, which is contained quadratically in relation (24).

5. CONCLUSIONS

We have shown that passively Q-switched microchip lasers using SESAM's are well described by a simple model from which we have derived handy equations for the basic parameters. Practical design guidelines were given that help in achieving different operating parameters. Using different absorbers with respect to the amount of saturable absorption, recovery time, and saturation intensity, we demonstrated pulse widths from 37 ps to 30 ns and repetition rates from 27 kHz to 7 MHz at peak powers of as much as 5 kW from Nd-doped microchip lasers and pulse energies of as much as 4 μJ with Er:Yb:glass microchip lasers. The short cavity length of microchip lasers combined with the semiconductor saturable absorber mirror led to what are to our knowledge the shortest single-frequency Q-switched pulses ever generated from a solid-state laser.

APPENDIX A

The model introduced in Subsection 2.A can be described with rate equations, which allow us to derive an analytical expression for the gain reduction. To have more insight into the time dependence of such dynamic parameters as gain, loss, and power, we numerically integrated the rate equations for a cw pumped four-level gain material. For integration we used the GEAR method[41] because the set of differential equations is rather stiff; i.e., the dynamics of the system occurs on time scales that differ by many orders of magnitude.

The rate equations are stated here in terms of experimentally relevant parameters such as the laser power $P(t)$, the intensity gain coefficient per cavity round trip $g(t)$, and the intensity saturable loss coefficient per cavity round trip $q(t)$. If we assume that all changes per cavity round trip are small, i.e., $g, q, l \ll 1$ and neglect the spontaneous emission into the laser mode, the rate equations are[42]

$$T_R \frac{\mathrm{d}P(t)}{\mathrm{d}t} = [g(t) - q(t) - l]P(t), \tag{A1}$$

$$\frac{\mathrm{d}g(t)}{\mathrm{d}t} = -\frac{g(t) - g_0}{\tau_L} - \frac{g(t)P(t)}{E_L}, \tag{A2}$$

$$\frac{\mathrm{d}q(t)}{\mathrm{d}t} = -\frac{q(t) - q_0}{\tau_A} - \frac{q(t)P(t)}{E_A}. \tag{A3}$$

Here T_R is the cavity round-trip time, E_L is the saturation energy of the gain [Eq. (3)], τ_L is the upper-state lifetime of the gain medium, E_A is the saturation energy of the absorber, and τ_A is the relaxation time of the absorber.

During the transit time of the pulse, the absorber relaxation and the pumping of the gain can be neglected. Then the peak power and the pulse width can be determined from the simplified set of rate equations for passive Q switching[19,42]

$$T_R \frac{\mathrm{d}P}{\mathrm{d}t} = (g - q - l)P, \tag{A4}$$

$$\frac{\mathrm{d}g}{\mathrm{d}t} = -\frac{gP}{E_L}, \tag{A5}$$

$$\frac{\mathrm{d}q}{\mathrm{d}t} = -\frac{qP}{E_A}. \tag{A6}$$

The division of Eq. (A6) by Eq. (A5) gives a relationship between saturable absorption $q(t)$ and gain $g(t)$ that can be integrated to express $q(t)$ as a function of $g(t)$ (Ref. 19):

$$q = q_0 (g/g_i)^{\beta}, \tag{A7}$$

where the initial conditions are initial gain g_i as given in Eq. (6) and an absorber in the ground state (Subsection 2.B). β is the ratio between the saturation energy of the gain and the saturation energy of the absorber:

$$\beta = E_L / E_A. \tag{A8}$$

As we mentioned in section 2, we typically have $\beta \gg 1$; i.e., in the 1-μm experiments discussed in Subsection 3.C, $\beta \approx 1000$.

Analogously, we can divide Eq. (A4) by Eq. (A5) and make use of Eq. (A7). Subsequent integration yields the (instantaneous) power as a function of the gain during the Q-switch cycle[19]:

$$P(g) = -\frac{E_L}{T_R}(g - g_i) + \frac{l E_L}{T_R} \ln\left(\frac{g}{g_i}\right) + \frac{E_A}{T_R} q_0 \left[\left(\frac{g}{g_i}\right)^{\beta} - 1\right]. \tag{A9}$$

This expression is equivalent to Eq. (6) of Ref. 19. If we neglect the last term in Eq. (A9), which is due to the saturable absorber, Eq. (A9) reduces to Eq. (17) of Ref. 39, where the case of a rapidly Q-switched laser is analyzed. By integrating Eq. (A9) one can get an expression for the pulse energy that is consistent with Eq. (5). With the help of the peak power [also from Eq. (A9)], the pulse energy, and an assumed sech^2 pulse, expression (9) can be derived.

To obtain an expression for the gain reduction of a Q-switched pulse we make use of Eq. (A9) and note that the power is approximately zero after the pulse [It is not exactly zero because, for this case, the power would remain zero forever according to Eq. (A1). A few seed photons that are due to spontaneous emission are always present to initiate the Q-switching process. But this number is orders of magnitude smaller than the typical photon number present in a Q-switched pulse.] The assumption of zero power after the pulse yields an expression for final gain coefficient g_f after the pulse and gain reduction Δg of the pulse:

$$P(g = g_f) = 0 = g_i - g_f + l \ln(g_f/g_i) + \frac{1}{\beta} q_0 [(g_f/g_i)^{\beta} - 1]. \tag{A10}$$

With Eqs. (4) and (6) and the approximation for a large saturation ratio β, Eq. (A10) yields a transcendental expression for Δg:

$$0 \approx \Delta g + l \ln\left(\frac{l + q_0 - \Delta g}{l + q_0}\right). \tag{A11}$$

Numerical solutions of relation (A11) for Δg as a function of l are plotted in Fig. 4 for several values of q_0. One can see that the approximation $\Delta g \approx 2q_0$ holds for values of q_0 up to $q_0 = l$ within 20%. Figure 5 shows numerical solutions of relation (A11) for Δg multiplied by the output coupling efficiency for fixed initial gain $g_i = l_{\mathrm{out}} + l_p + q_0$ and for $l_p = \gamma q_0$ for various proportionality factors γ. Maximum pulse energy is obtained for values of l close to $g_i/2$.

ACKNOWLEDGMENTS

We thank G. Huber for the Nd:LSB crystals. This research was supported by the Swiss Priority Program in Optics.

G. J. Spühler's e-mail address is spuehler @iqe.phys.ethz.ch.

REFERENCES

1. J. J. Zayhowski and A. Mooradian, "Single-frequency microchip Nd lasers," Opt. Lett. **14**, 24–26 (1989).
2. U. Keller, K. J. Weingarten, F. X. Kärtner, D. Kopf, B. Braun, I. D. Jung, R. Fluck, C. Hönninger, N. Matuschek, and J. Aus der Au, "Semiconductor saturable absorber mirrors (SESAMs) for femtosecond to nanosecond pulse generation in solid-state lasers," IEEE J. Sel. Top. Quantum Electron. **2**, 435–453 (1996).
3. U. Keller, D. A. B. Miller, G. D. Boyd, T. H. Chiu, J. F. Ferguson, and M. T. Asom, "Solid-state low-loss intracavity saturable absorber for Nd:YLF lasers: an antiresonant semiconductor Fabry–Perot saturable absorber," Opt. Lett. **17**, 505–507 (1992).
4. U. Keller, "Semiconductor nonlinearities for solid-state laser modelocking and Q-switching," in *Nonlinear Optics in Semiconductors*, A. Kost and E. Garmire, eds. (Academic, Boston, Mass., 1998), Vol. 59, Chap. 4, pp. 211–285.
5. Y. Shimony, Z. Burshtein, and Y. Kalisky, "Cr4+:YAG as passive Q-switch and Brewster plate in a pulsed Nd:YAG laser," IEEE J. Quantum Electron. **31**, 1728–1741 (1995).
6. J. J. Zayhowski and C. Dill III, "Diode-pumped passively Q-switched picosecond microchip lasers," Opt. Lett. **19**, 1427–1429 (1994).
7. B. Braun, F. X. Kärtner, M. Moser, G. Zhang, and U. Keller, "56-ps passively Q-switched diode-pumped microchip laser," Opt. Lett. **22**, 381–383 (1997).
8. R. Fluck, B. Braun, E. Gini, H. Melchior, and U. Keller, "Passively Q-switched 1.34-μm Nd:YVO_4 microchip laser using semiconductor saturable-absorber mirrors," Opt. Lett. **22**, 991–993 (1997).
9. R. Fluck, R. Häring, R. Paschotta, E. Gini, H. Melchior, and U. Keller, "Eyesafe pulsed microchip laser using semiconductor saturable absorber mirrors," Appl. Phys. Lett. **72**, 3273–3275 (1998).
10. R. W. Hellwarth, ed., *Advances in Quantum Electronics* (Columbia U. Press, New York, 1961).
11. F. J. McClung and R. W. Hellwarth, "Giant optical pulsations from ruby," J. Appl. Phys. **33**, 828–829 (1962).
12. R. J. Collins and P. Kisliuk, "Control of population inversion in pulsed optical masers by feedback modulation," J. Appl. Phys. **33**, 2009–2011 (1962).
13. A. A. Vuylsteke, "Theory of laser regeneration switching," J. Appl. Phys. **34**, 1615–1622 (1963).

14. W. G. Wagner and B. A. Lengyel, "Evolution of the giant pulse in a laser," J. Appl. Phys. **34**, 2040–2046 (1963).
15. L. E. Erickson and A. Szabo, "Effects of saturable absorber lifetime on the performance of giant-pulse lasers," J. Appl. Phys. **37**, 4953–4961 (1966).
16. L. E. Erickson and A. Szabo, "Behavior of saturable-absorber giant-pulse lasers in the limit of large absorber cross section," J. Appl. Phys. **38**, 2540–2542 (1967).
17. J. J. Zayhowski, "Q-switched operation of a microchip laser," Opt. Lett. **16**, 575–577 (1991).
18. J. J. Zayhowski and P. L. Kelley, "Optimization of Q-switched Lasers," IEEE J. Quantum Electron. **27**, 2220–2225 (1991).
19. J. J. Degnan, "Optimization of passively Q-switched lasers," IEEE J. Quantum Electron. **31**, 1890–1901 (1995).
20. J. J. Zayhowski, "Limits imposed by spatial hole burning on the single-mode operation of standing-wave laser cavities," Opt. Lett. **15**, 431–433 (1990).
21. B. Braun, K. J. Weingarten, F. X. Kärtner, and U. Keller, "Continuous-wave mode-locked solid-state lasers with enhanced spatial hole-burning. I. Experiments," Appl. Phys. B: Lasers Opt. **61**, 429–437 (1995).
22. J. J. Zayhowski, "Ultraviolet generation with passively Q-switched microchip lasers," Opt. Lett. **21**, 588–590 (1996).
23. J. J. Zayhowski, "Thermal guiding in microchip lasers," in *Advanced Solid-State Lasers,* H. P. Jenssen and G. Dube, eds., Vol. 6 of OSA Proceedings Series (Optical Society of America, Washington, D.C., 1990), pp. 9–14.
24. S. Longhi, "Theory of transverse modes in end-pumped microchip lasers," J. Opt. Soc. Am. B **11**, 1098–1107 (1994).
25. L. R. Brovelli, U. Keller, and T. H. Chiu, "Design and operation of antiresonant Fabry–Perot saturable semiconductor absorbers for mode-locked solid-state lasers," J. Opt. Soc. Am. B **12**, 311–322 (1995).
26. G. L. Witt, R. Calawa, U. Mishra, and E. Weber, eds., *Low Temperature (LT) GaAs and Related Materials* (Materials Research Society, Pittsburgh, Pa., 1992), Vol. 241.
27. Kigre, Inc., QX laser glasses data sheet (Kigre, Hilton Head Island, South Carolina, 1996).
28. B. Beier, J.-P. Meyn, R. Knappe, K.-J. Boller, G. Huber, and R. Wallenstein, "A 180-mW Nd:$LaSc_3(BO_3)_4$ single-frequency TEM_{00} microchip laser pumped by an injection-locked diode-laser array," Appl. Phys. B **58**, 381–388 (1994).
29. J.-P. Meyn, T. Jensen, and G. Huber, "Spectroscopic properties and efficient diode-pumped laser operation of neodymium doped lanthanum scandium borate," IEEE J. Quantum Electron. **30**, 913–917 (1994).
30. J.-P. Meyn, "Neodym-Lanthan-Scandium-Borat: Ein neues Material für miniaturisierte Festkörperlaser," Ph.D. dissertation (Universität Hamburg, Hamburg, Germany, 1994).
31. Casix, crystals and materials catalog (Casix, Inc., Fuzhou, Fujian, China).
32. P. Laporta, Politecnico de Milano, Dipartimento di Fisica, Piazza Leonardo da Vinci 32, 20133 Milano, Italy (personal communication, 1997).
33. W. Koechner, *Solid-State Laser Engineering* (Springer-Verlag, Berlin, 1992).
34. B. Braun, F. X. Kärtner, U. Keller, J.-P. Meyn, and G. Huber, "Passively Q-switched 180-ps Nd:LSB microchip laser," Opt. Lett. **21**, 405–407 (1996).
35. E. Snitzer and R. Woodcock, "Yb^{3+}–Er^{3+} glass laser," Appl. Phys. Lett. **6**, 45–46 (1965).
36. H. A. Haus, "Parameter ranges for cw passive modelocking," IEEE J. Quantum Electron. **12**, 169–176 (1976).
37. F. X. Kärtner, L. R. Brovelli, D. Kopf, M. Kamp, I. Calasso, and U. Keller, "Control of solid-state laser dynamics by semiconductor devices," Opt. Eng. (Bellingham) **34**, 2024–2036 (1995).
38. T. Taira, A. Mukai, Y. Nozawa, and T. Kobayashi, "Single-mode oscillation of laser-diode-pumped Nd:YVO_4 microchip lasers," Opt. Lett. **16**, 1955–1957 (1991).
39. A. E. Siegman, *Lasers* (University Science Books, Mill Valley, Calif., 1986).
40. J. R. Bettis, R. A. House II, and A. H. Guenther, "Spot size and pulse duration dependence of laser-induced damage," in *Laser Induced Damage in Optical Materials*, NBS Spec. Publ. **462**, 338–345 (1976).
41. L. O. Chua, *Computer Aided Analysis of Electronic Circuits: Algorithms and Computational Techniques* (Prentice-Hall, Englewood Cliffs, N.J., 1975).
42. A. Szabo and R. A. Stein, "Theory of laser giant pulsing by a saturable absorber," J. Appl. Phys. **36**, 1562–1566 (1965).